nanomaterials

MDPI

Article

$A_2AgCrBr_6$ (A = K, Rb, Cs) and Cs_2AgCrX_6(X = Cl, I) Double Perovskites: A Transition-Metal-Based Semiconducting Material Series with Remarkable Optics

Pradeep R. Varadwaj

Department of Chemical System Engineering, School of Engineering, The University of Tokyo 7-3-1, Tokyo 113-8656, Japan; pradeep@t.okayama-u.ac.jp or prv.aist@gmail.com

Received: 25 April 2020; Accepted: 15 May 2020; Published: 18 May 2020

Abstract: With an interest to quest for transition metal-based halogenated double perovskites $AB'B''X_6$ as high performance semiconducting materials for optoelectronics, this study theoretically examined the electronic structures, stability, electronic (density of states and band structures), transport (effective masses of charge carriers), and optical properties (dielectric function and absorption coefficients, etc.) of the series $A_2AgCrBr_6$ (A = K, Rb, Cs) using SCAN + $rVV10$. Our results showed that $A_2AgCrBr_6$ (A = Rb, Cs), but not $K_2AgCrBr_6$, has a stable perovskite structure, which was revealed using various traditionally recommended geometry-based indices. Despite this reservation, all the three systems were shown to have similar band structures, density of states, and carrier effective masses of conducting holes and electrons, as well as the nature of the real and imaginary parts of their dielectric function, absorption coefficient, refractive index, and photoconductivity spectra. The small changes observed in any specific property of the series $A_2AgCrBr_6$ were due to the changes in the lattice properties driven by alkali substitution at the A site. A comparison with the corresponding properties of Cs_2AgCrX_6 (X = Cl, I) suggested that halogen substitution at the X-site can not only significantly shift the position of the onset of optical absorption found of the dielectric function, absorption coefficient and refractive spectra of $Cs_2AgCrCl_6$ and Cs_2AgCrI_6 toward the high- and low-energy infrared regions, respectively; but that it is also responsible in modifying their stability, electronic, transport, and optical absorption preferences. The large value of the high frequency dielectric constants—together with the appreciable magnitude of absorption coefficients and refractive indices, small values of effective masses of conducting electrons and holes, and the indirect nature of the bandgap transitions, among others—suggested that cubic $A_2AgCrBr_6$ (A = Rb, Cs) and $Cs_2AgCrCl_6$ may likely be a set of optoelectronic materials for subsequent experimental characterizations.

Keywords: halide double perovskites; effect of chromium; stability; DOS and band structures; transport and optical properties; DFT studies

1. Introduction

Innovative materials that display impressive geometrical, stability, electronic, transport, and optical characteristics in the infrared through visible to ultraviolet region of the electromagnetic spectrum are a special class of semiconductors for application in optoelectronic devices [1–9]. Halide based single [10–17] and double perovskites [1–9,18–22] known by the chemical formulae ABX_3 and $AB'B''X_6$, respectively, are examples of such compounds. Not only do they absorb light, but many of them also emit light in specific regions of the electromagnetic spectrum, depending on the nature of ingredients at the atomic scale with which they are built. In single halide perovskites with ABX_3 composition [10,11], A is the organic or inorganic species in the +1 oxidation state (viz. $CH_3NH_3^+$,

$HC(NH_2)_2^+$, $C(NH_2)_3^+$, Cs^+, Na^+), X is the halogen derivative in the −1 oxidation state (viz. F^-, Cl^-, Br^-, I^-), and B = transition metal (d-block) or non-transition metal (p-block) element in the +2 oxidation state (viz. Pb^{2+}, Sn^{2+}, and Ge^{2+}). In halide double perovskites with *A*B'B''X_6 composition [1–9,18–24], the B' site is usually occupied with a monovalent transition metal or an alkali metal (e.g., Cu+, Ag+, and Na^+) and the B'' site is occupied with a transition metal or non-transition metal cation in the +3 oxidation state (e.g., Cr^{3+}, In^{3+}, Sb^{3+}, Bi^{3+}).

Although *A*BX_3 halide perovskites have been identified as best light absorbers with the largest PCE (power conversion efficiency) of 25.2% for $CH_3NH_3PbI_3$ [25], most of the halide-based double perovskites experimentally characterized to date were recognized as weak absorbers of light in the infrared and visible regions. $Cs_2AgBiBr_6$ is one of such largely studied halide double perovskites that found application in the development of solar cells [2,3]. Vacancy-ordered $A_2B^{4+}X_6$ halide double perovskites (viz. Cs_2TiBr_6) exhibit favorable bandgaps, with PCE can go up to 3.3% [4]. Whilst *A*B'B''X_6 exhibits low PCE (viz. 2.43% for $Cs_2AgBiBr_6$) [2,3], several of them have been demonstrated to behave as photodetectors. For instance, $Cs_2AgInCl_6$ is a single crystal-based UV detector that has displayed best performance with visible blind, low dark current (~10 pA at 5 V bias), fast photoresponse (~1 ms), high ON–OFF ratio (~500), and high detectivity (~1012 Jones) [2]. $Cs_2AgBiBr_6$ thin films were also regarded as photodetectors, as they exhibit high responsivity of 7.01 A W^{-1}, specific detectivity of 5.66×10^{11} Jones, and ON–OFF ratio of 2.16×10^4, among other impressive properties [5]. When $Cs_2AgBiBr_6$ is embedded in a polymer matrix, it can behave as an X-ray detector [6]. $Cs_2AgBiBr_6$ nanocrystals, as a photocatalyst, were used to conduct the CO_2 reduction reactions with high selectivity and stability. Similarly, the Bi-doped Cs_2SnCl_6 systems were identified as blue emissive phosphors, where Bi^{3+} is the luminescent dopant [7]. The $Cs_2(Ag_{0.60}Na_{0.40})InCl_6$ system optimally alloyed with 0.04% Bi^{3+} doping was shown to emit warm white light with 86 ± 5% quantum efficiency, working for over 1000 h [8,9].

Whereas the invention of *A*B'B''X_6 halide double perovskites has been known over decades [26–32], their importance as photovoltaic and luminescent materials has only recently been realized [1–9,18–24]. This came after the rationalization that lead-containing halide perovskites, such as $CH_2NH_3PbX_3$, are environmentally unfriendly and toxic, which can be easily decomposed when exposed to UV light, heat, water pressure, ambient air oxygen, etc. [33–36]. Therefore, thousands of halide double perovskites have been investigated using high-throughput screening to discover high performance materials for photovoltaic and optoelectronic applications [37–41]. For instance, *A*BiCuX_6 [A = Cs_2, $(MA)_2$, $(FA)_2$, CsMA, CsFA, MAFA; X = I, Br, Cl] were theoretically shown suitable for photovoltaic and optoelectronic applications [42]. In fact, dozens of such compounds have been synthesized using experimental methods and characterized [1–9,18–24]. Many of them were found to be environmentally stable and non-toxic. This is probably because the lead ion of *A*PbX_3 was replaced by a combination of monovalent and trivalent ions, or a tetravalent ion and a vacancy site, and that this arrangement also leads to the same overall charge balance expected of traditional halide perovskites [33–36]. As indicated above, the main problem associated with the experimentally known halogenated double perovskites is that most of them exhibited poor PCE and are not well suited for efficient solar cell designs. Therefore, experimental and theoretical studies on similar systems with different atomic compositions at the *A*, B', and B'' sites may lead to any large scale emergence of such materials, as such substitutions would assist not only in regulating the crystal structures and defects, but also in modifying their electronic, transport, and optical properties [38–43].

We are basically interested in the theoretical modeling of *A*B'B''X_6 systems, where the B''-site is a transition metal cation from the first and second rows of the periodic table. Substitution/doping at the B'' site by the trivalent transition metal cations (or by the non-transition metal cations) has already resulted in the synthetic development of Mn^- [44,45], Cu^- [46] and Cr-doped [23,24] $Cs_2AgInCl_6$, as well as of Yb- and Mn-doped Cs_2AgBiX_6 (X = Cl^-, Br^-) systems [47], with impressive (magneto) optoelectronics.

This study aims to investigate the geometric, electronic, transport, and optical properties of the series $A_2AgCrBr_6$ (*A* = K, Rb, Cs) using density functional theory. Our main interest lies in investigating

the traits of the first two heaviest members of the series, as commonly reported for similar systems with different B"-site species [1–9,18–24]. However, we extend our calculations for another lighter member of the series to deduce the extent to which the monovalent cation K at the *A* site can modify the geometric, electronic, and optical properties. The stability of the perovskite nature of $A_2AgCrBr_6$ is investigated using a set of geometry-based indices such as the octahedral factor [48], Goldschmidt's tolerance factor [49,50], global instability index [51,52], and the newly proposed tolerance factor [39]. We investigate the nature of orbital contribution of each atom type leading to the formation of the valence band maximum (VBM) and conduction band minimum (CBM). In addition, we investigate the optical properties [53–57]—e.g., the spectra of dielectric function, absorption coefficient, electrical conductivity, complex refractive index, and the Tauc plot—and compare them with those reported for similar perovskite systems. Finally, we perform similar calculations for Cs_2AgCrX_6 (X = Cl, I) to elucidate the character and magnitude of bandgap transitions and the extent to which halogen substitution at the X-site modifies the geometrical, stability, transport, and optoelectronic properties of $Cs_2AgCrBr_6$.

2. Computational Details

For reasons discussed in various previous studies [58–63], the geometries of $A_2AgCrBr_6$ (*A* = Cs, Rb, K) and Cs_2AgCrX_6 (X = Cl, I) were relaxed with SCAN + *rVV10* [58]. The SCAN functional is "strongly constrained and appropriately normed", which is paired with the non-local correlation part from the *rVV10* vdW density functional. It is one of the most suitable functionals recommended for the study the atomic structure of hybrid perovskite materials [63]. The k-point mesh $8 \times 8 \times 8$ centered at Γ was used for sampling the first Brillouin zone. The projector augmented-wave (PAW) method [64] was used. The energy cut-off used for geometry relaxation was 520 eV. The cut-off in total energy for the relaxation of the electronic degrees of freedom was set to 10^{-8} eV per cell, instead of the default value of 10^{-4}. A negative value of −0.01 for EDIFFG was set that defines the break condition for the ionic relaxation loop. The average forces on ions were minimized to 0.005 eV/Å. Dynamical and mechanical stabilities of the studied systems were not examined, as this may be the subject of another extensive study. All spin-polarization calculations, without considering the effect of spin-orbit coupling, were performed using VASP 5.4 [65,66].

The electronic band dispersions were calculated using the same functional SCAN + *rVV10* and the same band levels (Γ(0,0,0), X(1/2,0,1/2), L(1/2,1/2,1/2), W(*k* = 1/2,1/4,3/4)) of the Fm-$\bar{3}$m space group [67] previously used for $Cs_2InAgCl_6$ [43] were utilized. The density of states (DOS) was calculated with the tetrahedron method that incorporates Blöchl corrections [68]. The Pyband [69] and Sumo [70] packages were used to plot the DOS and band structures, respectively. To shed some light on the nature of mobility of charge carriers in $A_2AgCrBr_6$ (*A* = Cs, Rb, K) and Cs_2AgCrX_6 (X = Cl, I), the effective masses of electrons and holes (m_e^* and m_h^*, respectively) were calculated by parabolic fitting of the band edges. The relationship $m* = \pm\frac{\eta^2}{\frac{\partial^2 E(k)}{\partial k^2}}$ was invoked, where $E(k)$ is the energy of the band edge and the + and – signs refer the electrons and holes, respectively [71].

The frequency-dependent dielectric function ($\varepsilon(\omega)$) is one of the most important linear response functions often examined in the area of materials science and nanotechnology since it is the determinant of the optical properties of materials [53–57]. $\varepsilon(\omega)$ was calculated using Equation (1), where $\varepsilon_1(\omega) = \varepsilon_{\alpha\beta}^{(1)}(\omega)$ is the real part, and $\varepsilon_2(\omega) = \varepsilon_{\alpha\beta}^{(2)}(\omega)$ is the imaginary part of $\varepsilon(\omega)$.

$$\varepsilon(\omega) = \varepsilon_1(\omega) + i\varepsilon_1(\omega) = \varepsilon_{\alpha\beta}^{(1)}(\omega) + i\varepsilon_{\alpha\beta}^{(2)}(\omega) \quad (1)$$

$\varepsilon_{\alpha\beta}^{(1)}(\omega)$ is related to $\varepsilon_{\alpha\beta}^{(2)}(\omega)$ by the Kramers-Kronig transformation [53,72] and is given by Equation (2), where *P* denotes the principal value, and η is a small complex shift.

$$\varepsilon_{\alpha\beta}^{(1)}(\omega) = 1 + \frac{2}{\pi} P \int_0^{\infty} \frac{\varepsilon_{\alpha\beta}^{(2)}(\omega')\omega'}{\omega'^2 - \omega^2 + i\eta} d\omega' \quad (2)$$

$\varepsilon_{\alpha\beta}^{(2)}(\omega)$ was calculated using the Kubo-Greenwood formula given by Equation (3) [72], where subscripts in italics c and v refer to conduction and valence band states, respectively, and u_{ck} is the cell periodic part of the orbitals at the k-point k.

$$\varepsilon_{\alpha\beta}^{(2)}(\omega) = \frac{4\pi^2 e^2}{\Omega} \lim_{q\to 0} \frac{1}{q^2} \sum_{c,v,k} 2w_k \delta(\varepsilon_{ck} - \varepsilon_{vk} - \omega) \times \left\langle u_{ck+e\alpha q} \middle| u_{vk} \right\rangle \left\langle u_{vk+e\beta q} \middle| u_{vk} \right\rangle \quad (3)$$

The calculation of dielectric function has often been performed with dense k-point meshes, which is arguably because of the convergence of dielectric constant with respect the number of k-points leading to greater chemical accuracy [73]. Because of limited computational resources, we carried out such calculations using a 4 × 4 × 4 k-point mesh, in which, the number of empty conduction band states used was doubled and the number of grid points on which to compute DOS was set to a recommended value of 2000 [74]. Since the calculation of the linear response properties cannot be performed with the meta-GGA functional (SCAN + $rVV10$) using VASP 5.4 [65,66], we used the PBESol functional [75], in combination with the density functional perturbation theory (DFPT) method [76–78], to calculate such properties. The SCAN + $rVV10$ relaxed geometries of $A_2AgCrBr_6$ (A = Cs, Rb, K) and Cs_2AgCrX_6 (X = Cl, I) were used. Optical spectral properties, viz. photoabsorption coefficient $\alpha(\omega)$ [55], photoconductivity $\sigma(\omega)$ [57], refractive index $n(\omega)$ [54–56], and extinction coefficient $\kappa(\omega)$ [54–56] spectra were calculated using Equations (4)–(7), respectively.

$$\alpha(\omega) = \frac{\sqrt{2}\omega}{c} \left\{ \left[\varepsilon_1^2 + \varepsilon_2^2 \right]^{\frac{1}{2}} - \varepsilon_1(\omega) \right\}^{\frac{1}{2}} \quad (4)$$

$$\sigma(\omega) = \frac{4\varepsilon_0 E}{e} \varepsilon_2(\omega) \quad (5)$$

$$n(\omega) = \left[\frac{\sqrt{\varepsilon_1^2 + \varepsilon_2^2} + \varepsilon_1}{2} \right]^{\frac{1}{2}} \quad (6)$$

$$\kappa(\omega) = \left[\frac{\sqrt{\varepsilon_1^2 + \varepsilon_2^2} - \varepsilon_1}{2} \right]^{\frac{1}{2}} \quad (7)$$

In Equation (4), c and ω are the speed of light in vacuum and the frequency of light wave, respectively. In Equation (5), E is the energy of light in eV, ε_0 is the permittivity of vacuum in C^2/Nm^2, and e is the charge of electron in Coulomb. The calculated values of real and imaginary parts of $\varepsilon(\omega)$ were used for the calculation of optical constants given by Equations (4)–(7) [65,66].

3. Results and Discussion

3.1. Geometrical Properties and Stability of Perovskite Structures

Table 1 summarizes the calculated lattice constants (a, b, c, α, β, and γ), cell volume (V) and density (ρ) of $A_2AgCrBr_6$ (A = Cs, Rb, K). Figure 1a shows the relaxed polyhedral model of $Cs_2AgCrBr_6$, which is analogous with that found for $A_2AgCrBr_6$ (A = Rb, K). Because $a = b = c$ and α = β = γ for each of them, each adopts a 3D elpasolite structure with space group Fm-$\bar{3}$m.

Table 1. Selected lattice properties (lattice constants, volume, and density) and bandgaps of $A_2AgCrBr_6$ (A = K, Rb, Cs).

Compound	$a = b = c$/Å	$\alpha = \beta = \gamma$/Deg	Volume (V)/Å^3	ρ/gcm^{-3}	*GII*/v.u.	E_g/eV	Nature of E_g	E_g/eV	Nature of E_g
$Cs_2AgCrBr_6$	10.68	90	1217.10	4.94	0.02	1.27	Indirect at L→Γ	1.46	Direct at Γ
$Rb_2AgCrBr_6$	10.58	90	1182.56	4.55	0.06	1.28	Indirect at L→Γ	1.50	Direct at Γ
$K_2AgCrBr_6$	10.52	90	1165.60	4.09	0.08	1.29	Indirect at L→Γ	1.52	Direct at Γ

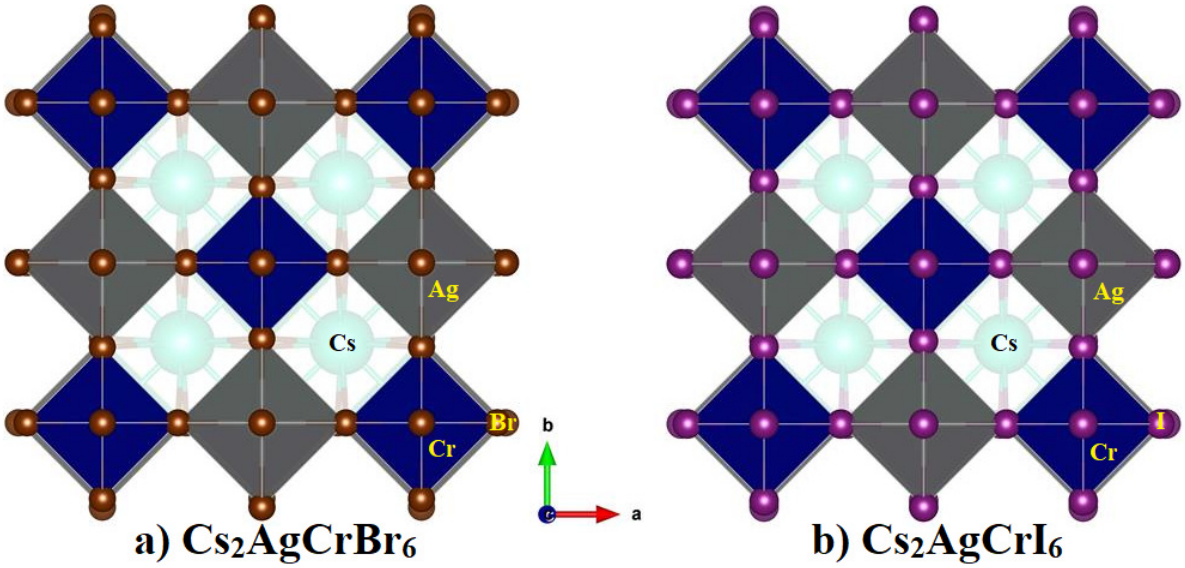

Figure 1. Comparison of the relaxed polyhedral model of (**a**) $Cs_2AgCrBr_6$ with (**b**) Cs_2AgCrI_6. Labeling of atom type is marked.

The lattice constant a is found to be the largest of 10.68 Å for $Cs_2AgCrBr_6$, and the smallest of 10.52 Å for $K_2AgCrBr_6$. The trend in the decrease of a in the series is consistent with the corresponding decrease in the cell volume V, with the V values ranging from 1217.10 Å^3 ($Cs_2AgCrBr_6$) to 1165.60 Å^3 ($K_2AgCrBr_6$). These changes are in agreement with the corresponding decrease in ρ, as well as that in the Ag–Cl, Cr–Cl, and A–Cl bond distances (Table 2), across the series passing from $Cs_2AgCrBr_6$ through $Rb_2AgCrBr_6$ to $K_2AgCrBr_6$. For comparison, our calculation on $Cs_2AgBiCl_6$ and $Cs_2AgBiBr_6$ yielded in lattice constants, density, and volumes that were not only close to experiment (within 2%), but also led to a suggestion that the Cr-substituted compounds are relatively lightweight, thus advocating the reliability of the accuracy of the DFT functional chosen.

The geometrical stability of $A_2AgCrBr_6$ was examined using the global instability index, *GII*, given by: $GII = \sqrt{\sum_{i=1}^{n} \frac{d_i^2}{n}}$, where n is the number of ions and d is the bond discrepancy factor defined as the deviation of bond valence sum (*BVS*) from formal valence [51,52]. *BVS* was calculated using the sum of bond valences (s_{ij}) around any specific ion given by: $BVS = \sum_{i=1}^{n} s_{ij}$, where $s_{ij} = \exp(\frac{l_0 - l_{ij}}{b})$, l_{ij} is a bond length, l_0 is the bond valence parameter empirically determined using experimental room-temperature structure data, and b is the bond softness parameter. For geometrically stable perovskite structures without steric distortions, *GII* equals 0.0 valence unit (v.u.); and for empirically unstable structures, *GII* > 0.2 v.u. [51,52].

Table 2. Comparison of selected bond distances r of $A_2AgCrBr_6$ (A = K, Rb, Cs) with Cs_2AgCrX_6 (X = Cl, I).

System	Bond Distances/Å		
	r(Ag–Br/I/Cl)	r(Cr–Br/I/Cl)	r(A–Br/I/Cl)
$Cs_2AgCrBr_6$	2.811	2.527	3.778
$Rb_2AgCrBr_6$	2.774	2.514	3.741
$K_2AgCrBr_6$	2.755	2.507	3.723
Cs_2AgCrI_6	2.977	2.761	4.059
$Cs_2AgCrCl_6$	2.697	2.369	3.586

The results of our calculation listed in Table 1 show that *GII* for $Cs_2AgCrBr_6$, $Rb_2AgCrBr_6$ and $K_2AgCrBr_6$ are 0.02, 0.06, and 0.08 v.u., respectively. This means that all the studied systems are associated with very marginal geometrical distortion compared to what might be expected of ideal perovskite structures. The largest instability is observed for $K_2AgCrBr_6$, which is believed to be due to the small size of the K^+ cation that causes the lattice $K_2AgCrBr_6$ to contract.

Table 3 lists Shannon's ionic radii of atoms that were used to understand the geometrical stability of $A_2AgCrBr_6$. Specifically, we used them for the calculation of the octahedral factor μ ($\mu = r_B/r_X$), and Goldschmidt tolerance factor ($t = \frac{r_A+r_X}{\sqrt{2}(r_B+r_X)}$). According to numerous previous demonstrations which have appeared in the literature [48–50], the combination (μ and t) should be suitable to assess the formability of perovskite structures provided μ and t values are in the ranges $0.414 < \mu < 0.732$ and $0.825 < t < 1.059$, respectively. Our calculation gave a value of 0.45 for μ for all $A_2AgCrBr_6$. Similarly, the t values for these systems were in the range $0.90 < t < 0.96$ (Table 3). Clearly, the combination (μ and t) recognizes the formability of $A_2AgCrBr_6$ (A = Cs, Rb, K) as stable perovskites. For comparison, the most studied $CH_3NH_3PbI_3$ was reported to have a t of 0.91 (unstable with respect to tilting), whereas NH_4PbI_3 has a t of 0.76 [79]. For the latter case, an alternative non-perovskite structure was suggested [79].

Table 3. Shannon's radii (r) of ions, octahedral factor (μ), Goldschmidt tolerance factor (t), and new tolerance factor (τ) *for* $A_2AgCrBr_6$ (A = Cs, Rb, K). The corresponding properties for Cs_2AgCrX_6 (X = Cl, I) are also included.

System	r_A/Å	$r[Ag^+]$/Å	$r[Cr^{3+}]$/Å	$r_B = [r(Ag^+) + r(Cr^{3+})]/2$/Å	Br^-/Å	$\mu = r_B/r_X$	t	τ
$Cs_2AgCrBr_6$	1.88	1.15	0.615	0.8825	1.96	0.45	0.96	4.04
$Rb_2AgCrBr_6$	1.72	1.15	0.615	0.8825	1.96	0.45	0.92	4.14
$K_2AgCrBr_6$	1.64	1.15	0.615	0.8825	1.96	0.45	0.90	4.22
$Cs_2AgCrCl_6$	1.88	1.15	0.615	0.8825	1.81	0.49	0.97	3.87
Cs_2AgCrI_6	1.88	1.15	0.615	0.8825	2.00	0.40	0.94	4.31

Table 3 also includes the τ (a newly proposed tolerance factor [39]) values for $A_2AgCrBr_6$. These were calculated using the relationship given by $\tau = \frac{r_X}{r_B} - n_A\left(n_A - \frac{\frac{r_A}{r_B}}{\ln(\frac{r_A}{r_B})}\right)$, where n_A is the oxidation state of A, r_i is the ionic radius of ion i, and $r_A > r_B$ by definition. The proposal to evaluate the geometrical stability of single and double perovskites (ABX_3 and $A_2B'B''X_6$, respectively) using τ ($\tau < 4.18$) was emerged after it was being realized that the recommended ranges for μ and t do not guarantee the formation of the perovskite structure since they give a high false-positive rate (51%) in the regions of t ($0.825 < t < 1.059$) and μ ($0.414 < \mu < 0.732$). In fact, τ was used to generalize outside of a 1034 training set of experimentally realized single and double perovskites (91% accuracy), and that its application was also useful to identify 23,314 new double perovskites ranked by their probability of being stable as perovskite [39]. Based on the criterion that $\tau < 4.18$ for geometrically stable perovskites, we found that $A_2AgCrBr_6$ (A = Cs, Rb) are a set of such geometrically stable perovskites ($4.04 < \tau < 4.14$), and $K_2AgCrBr_6$ ($\tau = 4.22$) is a partially unstable structure (a non-perovskite!), where the ionic radius of B

was calculated as the arithmetic mean of the ionic radii of *B*′ and *B*″. These results are not in exact agreement with that inferred from *GII* or the combination of μ and t values (see Tables 1 and 3). This may either mean that the value of τ ($\tau < 4.18$ [39]) recommended for identifying unknown perovskite structures may be stringent, causing the rejection of $K_2AgCrBr_6$ as a stable perovskite, or both the *GII* and the combination of μ and t mislead the stability features.

To understand the effect of halogen substitution at the X site of A_2AgCrX_6, we have carried out similar calculations only for Cs_2AgCrI_6 and $Cs_2AgCrCl_6$. The calculated lattice constants, cell volume, and density were 11.48 Å, 1511.9 Å^3, and 5.2 gcm^{-3} for Cs_2AgCrI_6, respectively. These were 10.13 Å, 1040.2 Å^3, and 4.08 gcm^{-3} for $Cs_2AgCrCl_6$, respectively. In other words, the halogen substitution does not cause significant strain in the lattice that can lead to the change in the symmetry of the system from Fm-$\bar{3}$m. However, the replacement of the Br atoms in $Cs_2AgCrBr_6$ by the Cl and I anions has indeed resulted in lattice contraction and expansion, respectively, which are expected to affect the electronic, transport, and optical properties of the resulting systems (*vide infra*). The presence of lattice contraction and expansion is also evident of metal-halide and alkali-halide bond lengths that are decreasing across the series in this order: $Cs_2AgCrCl_6 < Cs_2AgCrBr_6 > Cs_2AgCrI_6$. (A comparison detail of the Ag–X, Cr–X, and Cs–X bond distances for Cs_2AgCrX_6 (X = Cl, Br, I) is given in Table 2).

Moreover, the calculated μ and t values were 0.40 and 0.94 for Cs_2AgCrI_6 (Table 3), respectively. Based on the traditional arguments [48,50], one may not disapprove to call Cs_2AgCrI_6 a stable perovskite. The same argument applies to $Cs_2AgCrCl_6$, as the combination of the μ and t values (Table 3) favors a perovskite structure. This result is consistent with that inferred from the *GII* values (0.10 v.u. for $Cs_2AgCrCl_6$ and 0.00 v.u. for Cs_2AgCrI_6). However, our calculated τ value of 4.31, far exceeding its recommended value of 4.18, rejects Cs_2AgCrI_6 as a stable perovskite. This is analogously as τ rejected the $K_2AgCrBr_6$ system to be called a perovskite. However, this is not the case with $Cs_2AgCrCl_6$ ($\tau = 3.87$), in agreement with that reported recently [39]. Clearly, the aforesaid mismatch between the results associated with different indices suggests that the geometrical properties of a large body of $AB'B''X_6$ systems of different B′ and B″compositions, together with X = I and Br and A = K, need to be analyzed to reach any definitive conclusion on the predictability of *GII*- and τ-based stability features.

3.2. Density of States and Band Structures

Figure 2a–g shows the orbital-projected partial density of states of each atom type, and Figure 2h shows the atom projected partial density of states for $Cs_2AgCrBr_6$. From these, it may be said that the dispersion of the HOMO band (VBM) results collectively from contributions of e_g and t_{2g} states of both Ag (4d) and Cr(3d), and the 4p states of Br. This is also reminiscent of the data provided in Table 4, in which, the VBM is mainly due to the 4p states of Br (88%), and that the contribution from the 3d (Cr) and 4d (Ag) states is very small.

On the other hand, the LUMO band (CBM) of $Cs_2AgCrBr_6$ is predominantly of Cr (3d) character. It is substantially composed of the e_g orbital energy states (~72.5%). This, together with the small contributions from the Ag (5s) and Br (4p) states, causes the dispersion of the band. Note that alkali substitution at the A site has very little effect on the orbital characters of VBM and CBM. However, when the Br atom at the X-site was replaced by the I and Cl atoms, this had a very marginal effect on the orbital character of the CBM, and significant effect on the VBM. In particular, the 3d (Cr) energy states dominate below the Fermi level for $Cs_2AgCrCl_6$ (46%), which was comparatively larger than those arose from the 3p (35.2%) and 4d (17.0%) states of Cl and Ag, respectively. For Cs_2AgCrI_6, the I(5p) states dominate below the Fermi level, and the 3d (Cr) and 4d (Ag) states contribute marginally to the VBM. Figure 3 compares the nature of band dispersion of $Cs_2AgCrBr_6$ with Cs_2AgCrI_6, and Figure 4 illustrates the orbital- and atom-projected partial density of states for Cs_2AgCrI_6.

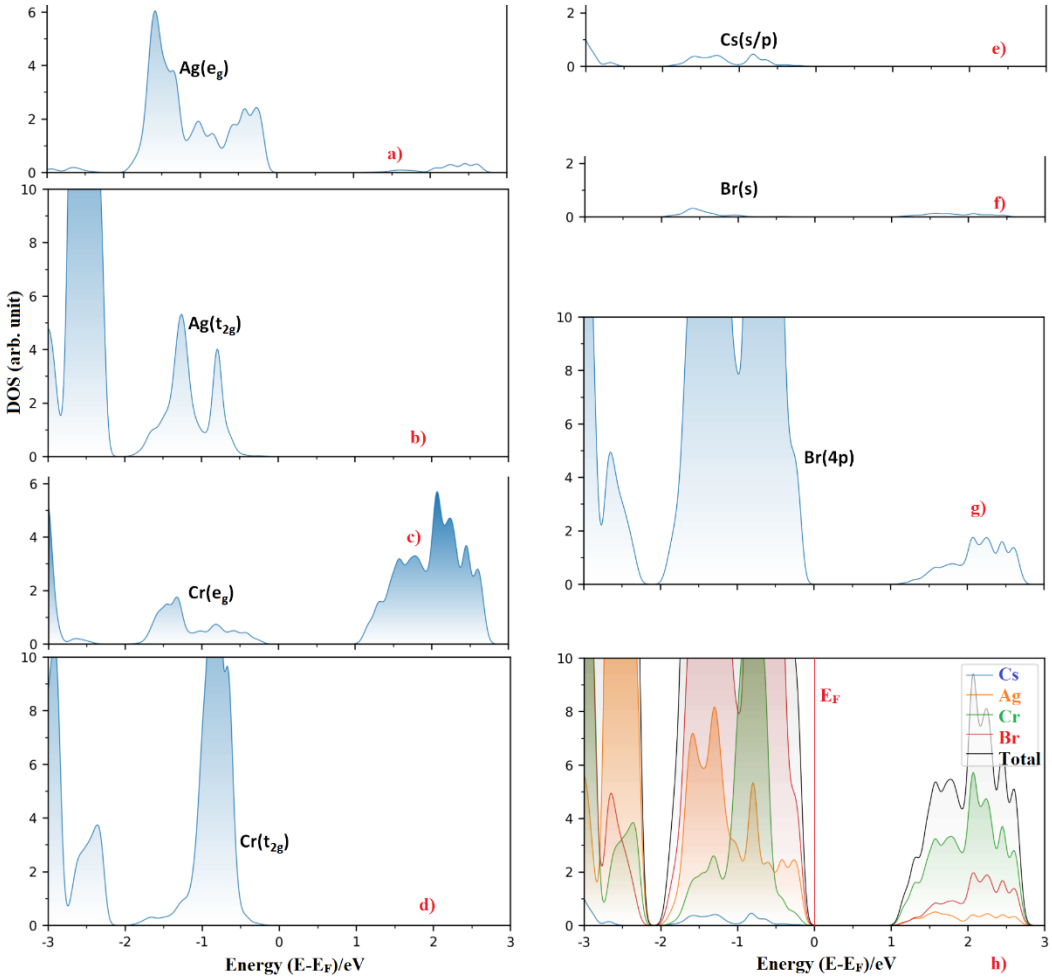

Figure 2. (**a**–**g**) The orbital-projected partial density of states of selective atom type for $Cs_2AgCrBr_6$. Included in (**h**) is the atom-projected density of states for the corresponding system. The Fermi level E_F is marked at 0 eV in (h).

Table 4. Normalized orbital contribution of selective atoms leading to the formation of VBM and CBM of $A_2AgCrBr_6$ (A = K, Rb, Cs). Given are also the corresponding contributions responsible for the band edges of Cs_2AgCrI_6 and $Cs_2AgCrCl_6$. Values in %.

	VBM			**CBM**		
	Cr 3d	Ag 4d	Br/I/Cl 4p/5p/3p	Cr 3d	Ag 5s	Br/I/Cl 4p/5p/3p
$Cs_2AgCrBr_6$	0.7	10.1	87.8	72.5	9.1	10.9
$Rb_2AgCrBr_6$	0.8	10.8	87.1	72.5	8.9	10.6
$K_2AgCrBr_6$	0.9	11.1	86.6	72.4	8.8	10.5
Cs_2AgCrI_6	7.95	2.82	86.8	69.9	8.9	12.7
$Cs_2AgCrCl_6$	46.0	17.0	35.2	74.9	10.1	9.4

From the bandgap (E_g) data listed in Table 1, it is apparent that the $A_2AgCrBr_6$ systems are an indirect bandgap material. This is arguably because the VBM is located at the high symmetry L-valley (VBM) and the CBM is located at the Γ-valley (CBM); see Figure 3a for $Cs_2AgCrBr_6$. The calculated bandgaps (E_g) of $A_2AgCrBr_6$ were found between 1.27 and 1.29 eV (Table 1), thereby suggesting the semiconducting nature of these materials. Small variations in E_g across the alkali series indicate that alkali substitution at the A-site of $A_2AgCrCl_6$ does not significantly affect the gap between CBM and

VBM, and is consistent with the nature and extent of orbital characters that were involved in the formation of these bands (Table 4).

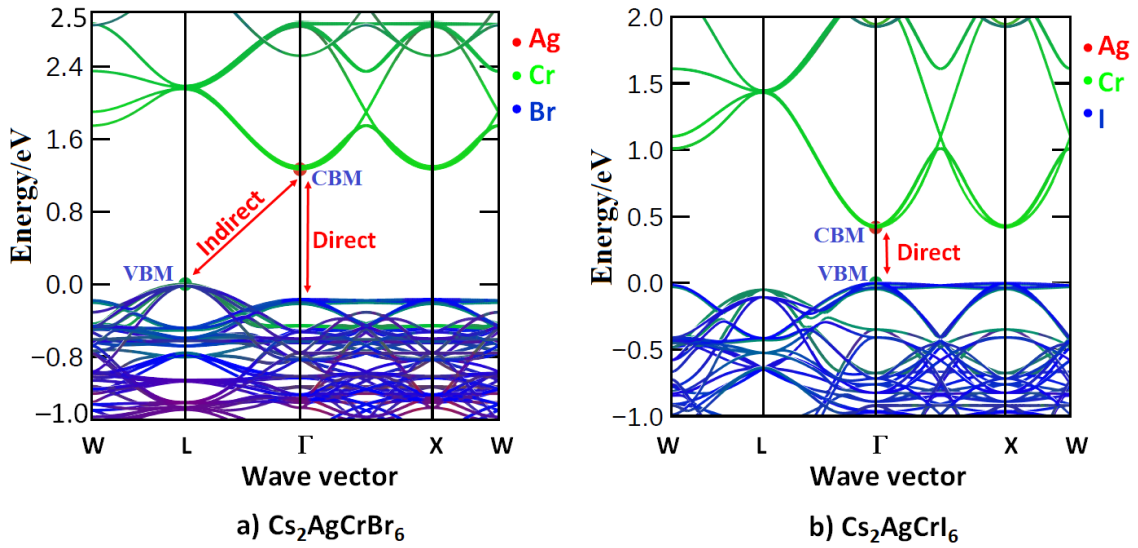

Figure 3. Comparison of the electronic band dispersion of (**a**) $Cs_2AgCrBr_6$ with (**b**) Cs_2AgCrI_6. The nature of band dispersion shown in (**a**) is virtually identical with those of $A_2AgCrBr_6$ (A = Rb, K) (not shown). The indirect nature of the bandgap with the VBM at the L- and Γ-points in (**a**) are also marked and Table 1 lists the E_g values for $Cs_2AgCrBr_6$. The conventional unit-cell geometries were used to calculate the band dispersion.

By contrast, Cs_2AgCrI_6 has a bandgap of 0.43 eV, and is direct at the Γ-valley (Figure 3b). Obviously, the replacement of the Br atoms of $Cs_2AgCrBr_6$ with iodine atoms not only causes the shift of the VBM from the L-valley to appear at the Γ-valley, but also significantly narrows the gap between the CBM and VBM and alters the character of the electronic transition between them. This is not the case with $Cs_2AgCrCl_6$ since the bandgap for this system is increased giving rise to an E_g value of 1.84 eV (SCAN + *rVV*10) and was indirect between the L-valley (VBM) and Γ–valley (CBM). These results lead to a conclusion that halogen substitution from Cl through Br to I at the X-site of Cs_2AgCrX_6 not only triggers the nature of the bandgap from indirect to direct, but also adjusts its magnitude from 1.84 eV to 0.43 eV.

In any case, the charge transport properties of any semiconducting material are strongly dependent on the effective masses of the charge carriers [80–82]. Table 5 summarizes the effective masses of conduction electrons and holes for $A_2AgCrBr_6$, which were calculated by parabolic fitting of the lower conduction band and the upper valence band centered at the Γ- and L-valleys, respectively. Since the HOMO band is formed by several spin-up and spin-down channels (total eight) caused by the Cr^{3+} ions, there are spin-up and spin-down holes along the crystallographic directions. The most important of these is the L→Γ direction, which is linked directly with the electronic transition between the VBM and CBM. As can be seen from Table 5, the effective masses of the spin-up holes (m_h*(*up*)) are always lighter than that of the spin-down holes (m_e*(*down*)), regardless of the nature of the *A*-site in $A_2AgCrBr_6$. This means that (m_h*(*down*)) would play an insignificant role in determining the transport phenomena that are usually governed by the band structures at and around the close vicinity of the Γ-point. In contrary, there are only spin-up electrons that are associated with the bottom of the conduction band. They are indeed small (m_e*(*up*) (values lie between 0.50 and 0.62 m_0 for all directions), but are not always heavier than those of m_h*(*up*). These results suggest that the studied systems might be suitable as hole (and electron) transporting materials due to their high mobility [81–83]. A similar result was found for $Cs_2AgCrCl_6$ (values not given).

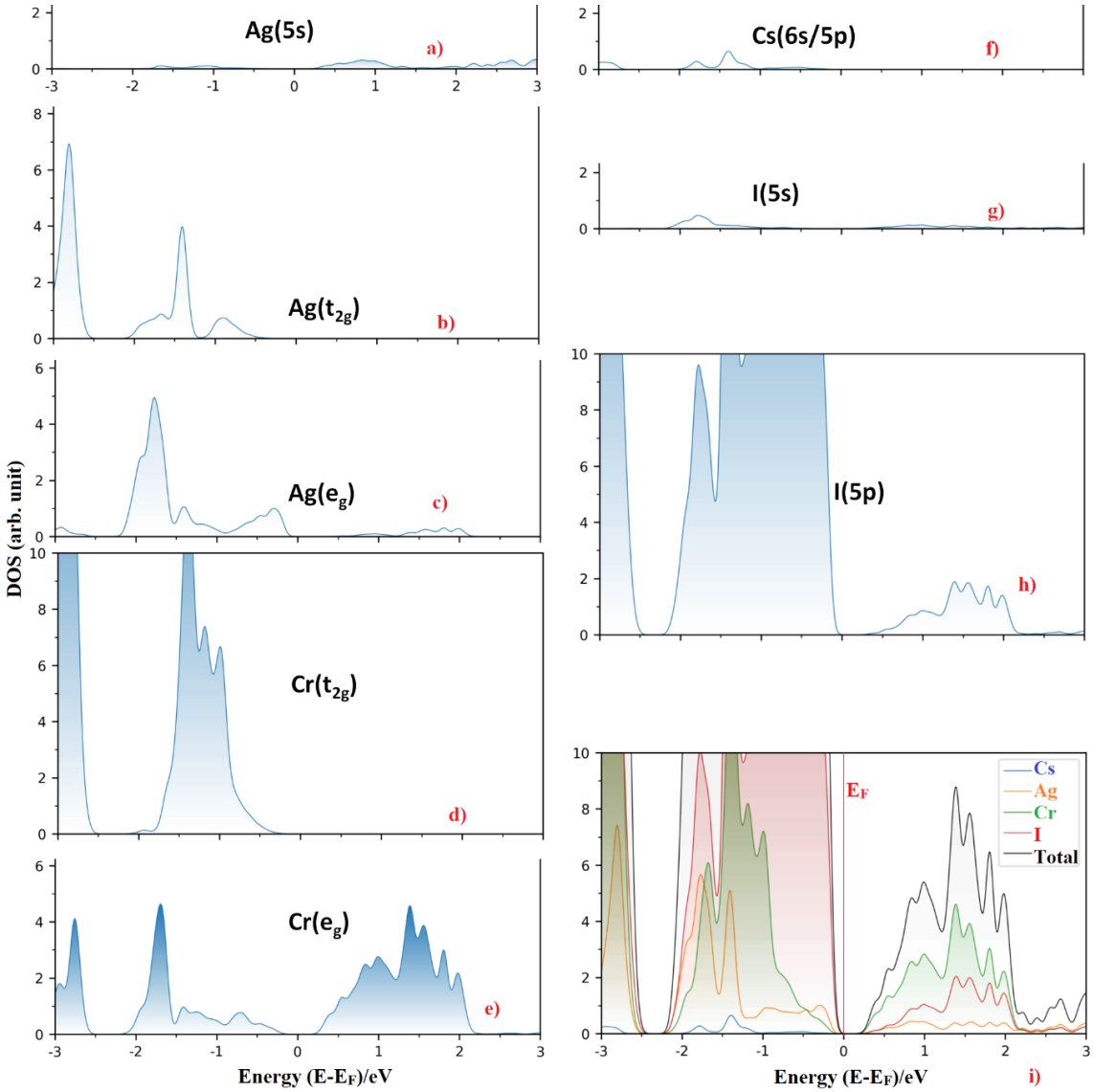

Figure 4. (**a**–**h**) The orbital-projected partial density of states of selected atom type for Cs_2AgCrI_6. Included in (**i**) is the atom-projected density of states for the corresponding system. The Fermi level E_F is marked at 0.0 eV.

Table 6 collects the $m_e^*(up)$ and $m_h^*(up)$ values for Cs_2AgCrI_6. Of the three, two channels associated with the top of the valence band are having significantly smaller $m_h^*(up)$ values along both the crystallographic directions (Γ→L and Γ→X) compared to that of the third one. $m_e^*(up)$ is always smaller than $m_h^*(up)$ regardless of the nature of crystallographic directions, which is obviously due to the 'flatter' nature of the VBM compared to the parabolic CBM (Figure 3b).

For comparison, Wang et al. have reported unusually heavier effective masses for holes for the hybrid perovskite series, $AEQTBX_4$ (B = Pb, Sn; X = Cl, Br, I; AEQT= $H_3NC_2H_4C_{16}H_8S_4C_2H_4NH_3^{2+}$), with the m_h^* values between 0.63 m_0 ((AEQT)SnI_4) and 105.21 m_0 ((AEQT)PbI_4) [84]. (AEQT)SnI_4 was observed to exhibit dispersive VBM and CBM, and was accompanied by a moderate fundamental bandgap of 2.06 eV involving a strong direct valence band to conduction band transition. This, together with the relatively light effective masses for electrons and holes (~0.6 m_0), and high dielectric constants, has led to a suggestion that this system is suitable for application as a top absorber of the tandem solar cell.

Table 5. Effective masses of charge carriers (holes and electrons) for $A_2AgCrBr_6$ (A = Cs, Rb, K) [a].

Compound	Property	Crystallographic Directions															
		L→W	L→Γ	L→W	L→Γ	L→W	L→Γ	L→W	L→Γ	L→W	L→Γ	L→W	L→Γ	L→W	L→Γ	L→W	L→Γ
$Cs_2AgCrBr_6$	m_h^*/m_0 (*up*)	−0.33	−0.47	−0.33	−0.47	−0.47	−0.47	−0.47	−0.57	−0.91	−0.56	−0.91	−0.57	−1.23	−0.84	−1.23	−0.85
	m_h^*/m_0 (*down*)	−0.33	−3.79	−0.33	−4.23	−0.47	−4.23	−0.47	−5.14	−0.91	−4.49	−0.91	−4.79	−1.23	−5.99	−1.23	−7.19
		Γ→L	Γ→X														
	m_e^*/m_0	0.50	0.59														
		L→W	L→Γ	L→W	L→Γ	L→W	L→Γ	L→W	L→Γ	L→W	L→Γ	L→W	L→Γ	L→W	L→Γ	L→W	L→Γ
$Rb_2AgCrBr_6$	m_h^*/m_0 (*up*)	−0.32	−0.45	−0.32	−0.46	−0.43	−0.46	−0.43	−0.54	−0.87	−0.53	−0.87	−0.53	−1.10	−0.73	−1.10	−0.73
	m_h^*/m_0 (*down*)	−0.32	−3.86	−0.32	−4.07	−0.43	−4.07	−0.43	−4.89	−0.87	−4.07	−0.87	−4.31	−1.10	−4.89	−1.10	−6.11
		Γ→L	Γ→X														
	m_e^*/m_0	0.50	0.60														
		L→W	L→Γ	L→W	L→Γ	L→W	L→Γ	L→W	L→Γ	L→W	L→Γ	L→W	L→Γ	L→W	L→Γ	L→W	L→Γ
$K_2AgCrBr_6$	m_h^*/m_0 (*up*)	−0.32	−0.45	−0.32	−0.45	−0.41	−0.45	−0.41	−0.52	−0.85	−0.52	−0.85	−0.52	−1.06	−0.68	−1.06	−0.68
	m_h^*/m_0 (*down*)	−0.32	−3.70	−0.32	−3.90	−0.41	−4.11	−0.41	−4.63	−0.85	−4.11	−0.85	−4.11	−1.06	−4.63	−1.06	−5.69
		Γ→L	Γ→X														
	m_e^*/m_0	0.50	0.61														

[a] m_h^* and m_e^* in units of electron rest mass m_0 ($m_0 = 9.11 \times 10^{-31}$ kg).

Table 6. Effective masses of conducting electrons and holes for Cs_2AgCrI_6 [a]

System		Γ→L	Γ→X	Γ→L	Γ→X	Γ→L	Γ→X
Cs_2AgCrI_6	m_h^*/m_0 (*up*)	−0.64	−0.52	−0.64	−0.52	−1.25	−12.96
	m_e^*/m_0 (*up*)	0.35	0.48				

[a] m_h^* and m_e^* in in units of electron rest mass m_0 ($m_0 = 9.11 \times 10^{-31}$ kg).

3.3. Optical Properties

The excitonic effect is generally approximated by solving the Bethe–Salpeter equation for the two-body Green's function, without or with considering local field effect [85]. Due to the high computational cost and limited computed resources, the frequency-dependent complex dielectric function was calculated within the framework of DFPT without taking into account the electron-hole coupling effect. Studies have shown that neglecting electron-hole coupling can yield reasonable results for semiconductors with small band gaps [86,87]. Nevertheless, Figure 5 shows the plot of the real and imaginary parts of the dielectric function as a function of photon energy for $A_2AgCrBr_6$. The first peak of the ε_2 curve is located at an energy higher than that of the ε_1 curve, and alkali substitution at the *A*-site causes a slight fluctuation in the high frequency dielectric behavior. For instance, these peaks on the ε_1 and ε_2 curves are positioned at energies of 1.45 and 1.63 eV for $Cs_2AgCrBr_6$, respectively. These are 1.53 and 1.72 eV for $Rb_2AgCrBr_6$, respectively, and are 1.55 and 1.74 eV for $K_2AgCrBr_6$, respectively. Similarly, the low frequency limit of the isotropically averaged value of ε_1 ($\omega = 0$) = ε_∞ (called optical dielectric constant or high-frequency dielectric constant) is found to be 6.1 for $Cs_2AgCrBr_6$, 5.4 for $K_2AgCrBr_6$, and 5.8 for $K_2AgCrBr_6$. This result indicates that the contribution of electrons to the static dielectric constant is appreciable and that the studied systems contain ionic bonds. Zakutayev et al. [88], as well as others [84], have previously demonstrated that perovskites with appreciable dielectric constants are defect tolerant. For comparison, $MAPbI_3$ (X = Cl, Br, I), and other perovskite systems [73] were reported to have virtually similar optical dielectric constants (viz. ε_∞ = 6.5 for $MAPbI_3$, 5.2 for $MAPbBr_3$, 4.2 for $MAPbCl_3$, and 5.3 for $CsPbI_3$).

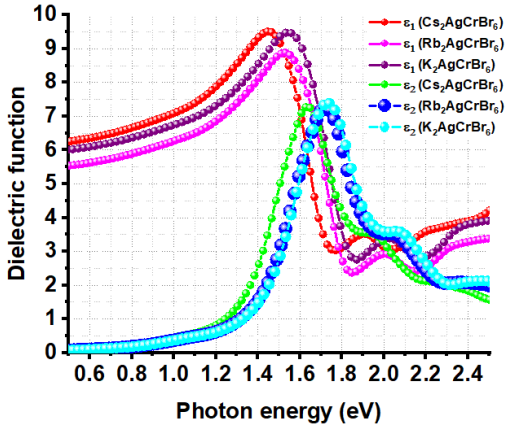

Figure 5. Illustration of the dependence of the real and imaginary parts (ε_1 and ε_2, respectively) of the dielectric function ε on the photon energy for $A_2AgCrBr_6$ (*A* = Cs, Rb, K) double perovskites.

The magnitude of the bandgap is the determinant of the onset of first optical absorption, which can be approximated using the spectra of ε_2. As such, the onset of absorption is approximately lying between 1.15 and 1.40 eV for $A_2AgCrBr_6$ (Figure 5), showing an appreciable absorption mostly in the infrared spectral region. Note that the bandgaps of $A_2AgCrBr_6$ evaluated using SCAN + *rVV*10 were lying between 1.27 and 1.29 eV, and the dielectric functions were calculated using PBEsol in conjunction with DFPT, yet there is a close match between bandgap and onset of optical absorption evaluated using the two different theoretical approaches employed.

Figure 6a,b compares the energy dependence of ε_1 and ε_2 for Cs_2AgCrX_6 (X = Cl, Br, I), respectively. From either of the two plots, it is apparent that halogen replacement has a significant effect not only on the magnitude of ε_∞, but also on the onset of optical absorption. For instance, the value of ε_∞ inferred from Figure 6a is approximately around 4.5, 6.1, and 8.9 for $Cs_2AgCrCl_6$, $Cs_2AgCrBr_6$, and Cs_2AgCrI_6, respectively. These indicate that Cs_2AgCrI_6 has a greater ability to screen charged defects compared to $Cs_2AgCrBr_6$ and $Cs_2AgCrCl_6$ [89,90]. The observed trend in the increase of ε_∞ caused by halogen substitution at the X-site in Cs_2AgCrX_6 is consistent with that reported for the $MAPbX_3$ (X = Cl, Br, I) series [73].

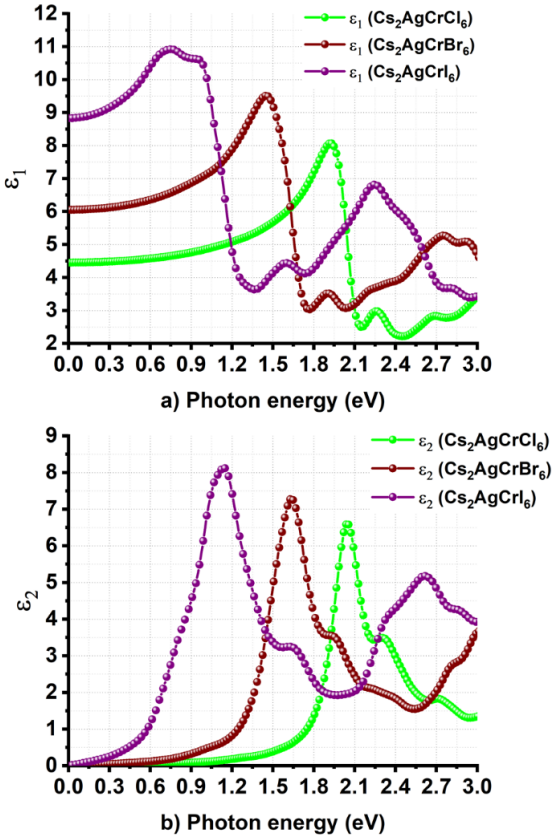

Figure 6. Nature of dependence of the (**a**) real and (**b**) imaginary part of dielectric function on the photon energy for Cs_2AgCrX_6 (X = Cl, Br, I).

The onset of optical absorption corresponding to the ε_2 spectra is positioned around 1.55 eV for $Cs_2AgCrCl_6$. This is significantly shifted from the near-infrared region to the low energy infrared region of the electromagnetic spectrum caused by the halogen substitution at the X-site, thus showing up at energies around 1.15 eV and 0.45 eV for $Cs_2AgCrBr_6$ and Cs_2AgCrI_6, respectively. These values are close to their corresponding bandgaps predicted using the SCAN + *rVV*10 functional. It is worth noting that we did not calculate the contribution of dielectric constant due to ions to the static dielectric constant, thus it is not possible to provide views on the polarity of the chemical bonds and the softness of the vibrations [91], as well as the nature and importance of (picosecond) response of lattice vibrations (phonon modes) that explain the ionic and lattice polarizations, and the extent to which the material would control the photovoltaic performance [74,89,90,92].

In any case, the major peaks in the ε_2 curve of $Cs_2AgCrCl_6$ are positioned at energies of 2.0 and 2.3 eV, whereas the onset of the optical absorption was located at an energy of 1.55 eV (Figure 6b). These peaks in the UV/Vis/NIR diffuse reflectance spectrum were experimentally observed at energies of 1.6 and 2.2 eV for hexagonal $Cs_2AgCrCl_6$, respectively, and were assigned to the d-d transitions of $^4A_2 \rightarrow {}^4T_2$ and $^4T_2 \rightarrow {}^4T_1$, respectively. This is not surprising given that the ground state of the

Cr^{3+} ($t_{2g}{}^3e_g{}^0$) cation in an octahedral O_h symmetry is described by $^4A_{2g}(F)$, and is accompanied with spin-allowed transitions from the $^4A_{2g}(F)$ ground state to the excited $^4T_2$ and $^4T_1$ states (that is, $^4T_2 \rightarrow {}^4T_1$ and $^4A_2 \rightarrow {}^4T_1$). Such d–d transitions were reported to occur at energies of 3.06 eV (405 nm) and 2.25 eV (550 nm) in the UV–vis spectrum of isolated Cr^{3+} complex of aspartic acid, respectively [93]. The intense and broad bands observed at energies of 2.93 eV and 2.13 eV for strontium formate dehydrate crystal of Cr^{3+} were attributed to the corresponding transitions, respectively [94]. Also, zinc-tellurite glasses doped with Cr^{3+} ion feature two intense broad bands with maxima at 454 nm (2.73 eV) and 650 nm (1.91 eV), which were assigned to the transitions $^4A_2 \rightarrow {}^4T_1$ and $^4A_2 \rightarrow {}^4T_2$, respectively [95]. In $Cs_2AgInCl_6$:Cr^{3+} halide double perovskite, the absorptions peaks at 1.55 eV (800 nm) and 2.19 eV (565 nm) were assigned to the same spin-allowed transitions $^4A_2 \rightarrow {}^4T_2$ and $^4T_2 \rightarrow {}^4T_1$, respectively. Because the VBM is dominated with Br(4p) and I(5p) energy states for $Cs_2AgCrBr_6$ and Cs_2AgCrI_6, respectively, and the contribution of Cr(3d) orbitals states to the VBM is reasonably small, the two electronic transitions appear in the ε_2 spectra in the region 0.3–2.2 eV were shifted toward the low energy regions (Figure 6b).

Figure 7 displays the plot of the absorption coefficient, photoconductivity, and complex refractive index for $A_2AgCrBr_6$. Equations (4)–(7) were used, respectively. Figure 7b shows the Tauc plot. These plots replicate the oscillator peaks of the dielectric function ε_2 in the region 0.0–3.0 eV (Figure 6). From Figure 7a, it is obvious that α for $A_2AgCrBr_6$, which determines the extent to which light of a particular energy can penetrate a material before it is absorbed [96], is non-zero (positive) both in the infrared and visible regions. As can be seen, different regions have different absorption coefficients. This may not be unusual given that the absorption coefficients of $MAPbI_3$ as low as 10^{-14} cm^{-1} were detected at room temperature for long wavelengths, and were 14 orders of magnitude lower than those observed at shorter wavelengths [97]. Nevertheless, α increases as the light energy increases and becomes a maximum at the strongest peak occurred at an energy around 1.7 eV for $Cs_2AgCrBr_6$. The trend in α in the series $A_2AgCrBr_6$ follows the order: $Cs_2AgCrBr_6$ (3.3×10^5 cm^{-1}) < $Rb_2AgCrBr_6$ (3.6×10^5 cm^{-1}) ≈ $K_2AgCrBr_6$ (3.6×10^5 cm^{-1}). These are somehow larger than those of 0.5×10^4 cm^{-1} and 1.5×10^4 cm^{-1} observed at 1.77 eV (700 nm) and 2.25 eV (550 nm) for $MAPbI_3$, respectively [98,99].

The nature of the curves of α is similar to that found for σ at the strongest peak positions in the region 0.0–2.5 eV (see Figure 7a vs. Figure 7c). The value of σ at these peaks is 2.64×10^9 Sm^{-1} for $Cs_2AgCrBr_6$, 2.76×10^9 Sm^{-1} for $Rb_2AgCrBr_6$, and 2.84×10^9 Sm^{-1} for $K_2AgCrBr_6$. For comparison, the average value of σ for $MAPbI_3$ thin films was reported to be 6×10^5 Sm^{-1} [100].

The above trend both in α and σ is not exactly similar to that found for the static refractive index n ($\omega = 0$), with the latter were around 2.5, 2.3, and 2.4 for $Cs_2AgCrBr_6$, $Rb_2AgCrBr_6$, and $K_2AgCrBr_6$, respectively (Figure 7d). The $n(\omega)$ values increase with respect to the increase of photon energy in the region 0.0–3.0 eV. The maximum of n at the highest peak in the region 0.0–3.0 eV varies between 3.0 and 3.2 for $A_2AgCrBr_6$.

Cl and I substitutions at the X-site in Cs_2AgCrX_6 has resulted in a relatively smaller α of 2.4×10^5 cm^{-1} for Cs_2AgCrI_6 and a relatively larger α of 4.0×10^5 cm^{-1} for $Cs_2AgCrCl_6$; all within the range 0.0–2.5 eV (Figure 8a). Although the peaks in the α spectrum of $Cs_2AgCrCl_6$ are relatively sharper than those of $Cs_2AgCrBr_6$ and Cs_2AgCrI_6, the different absorption edges found for the three systems are consistent with the corresponding bandgap properties. Also, the trend in α is concordant with the conductivity spectra shown in Figure 8b, in which, σ decreases in the series in this order: Cs_2AgCrI_6 < $Cs_2AgCrBr_6$ < $Cs_2AgCrCl_6$. On the other hand, the n ($\omega = 0$) values were 2.1, 2.5, and 3.0 for $Cs_2AgCrCl_6$, $Cs_2AgCrBr_6$, and Cs_2AgCrI_6, respectively (Figure 9a). The maximum values of n were approximately 2.9, 3.2, and 3.4 for the corresponding systems, respectively, a feature which is consistent with the trend in the optical dielectric constants (see above). Regardless of the nature of the A_2AgCrX_6 systems examined, the extinction coefficient (imaginary part of the refractive index) was found to be very small (Figures 7d and 9b), and is expected for semiconducting materials [101]. These results lead to a meaning that the studied Cs_2AgCrX_6 (X = Cl, Br, I) perovskites may result in relatively larger reflection at the perovskite/electrode interface. For comparison, the refractive indices

of $CH_3NH_3PbI_{3-x}Cl_x$ perovskite thin films were reported approximately to be 2.4 and 2.6 in the visible to near-infrared wavelength region [101]. He et al. have examined bulk single crystals of $CH_3NH_3PbX_3$ (CH_3NH_3 = MA, X = Cl, Br, I) and have measured refractive indices that rank in this order: $MAPbI_3$ > $MAPbBr_3$ > $MAPbCl_3$ at the same wavelength [102]. These results indicate that n may play an important role in determining the optical response properties of halide perovskites, which may serve as a useful metric in the parameter space for use in optoelectronic device design.

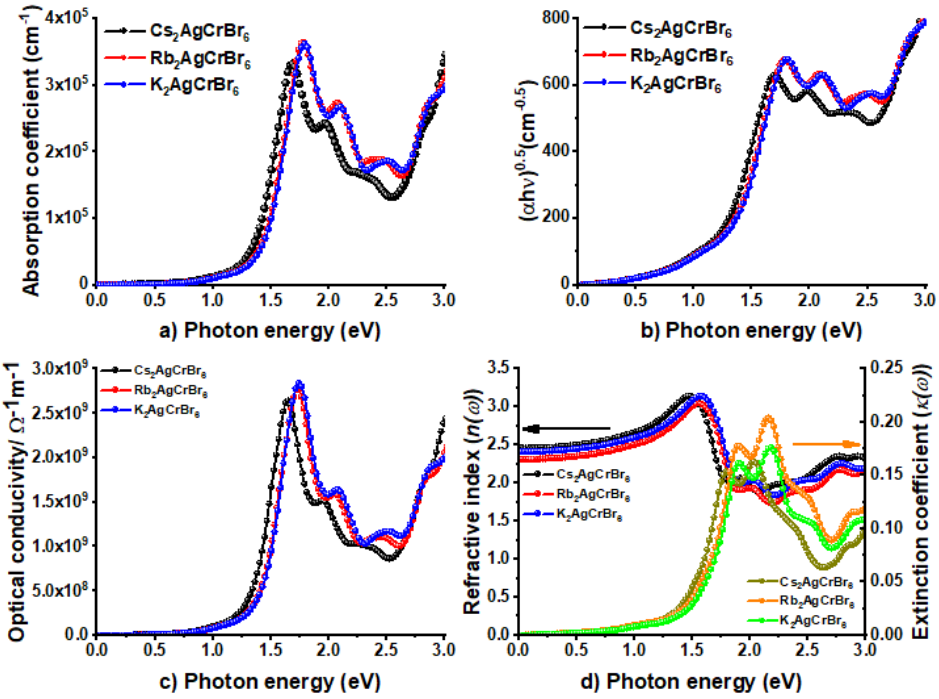

Figure 7. Illustration of the dependence of (**a**) absorption coefficient ($\alpha(\omega)$), (**b**) Tauc plot, (**c**) optical conductivity ($\sigma(\omega)$), and (**d**) the real and imaginary parts of refractive index (n and κ, respectively) on the photon energy for $A_2AgCrBr_6$ (A = Cs, Rb, K).

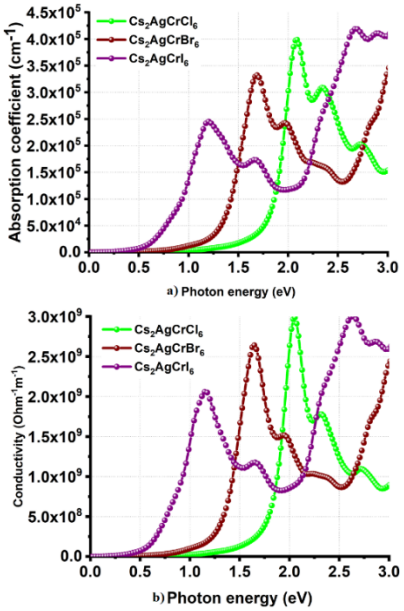

Figure 8. Behavior of the (**a**) absorption coefficient and (**b**) photoconductivity against photon energy for Cs_2AgCrX_6 (X = Cl, Br, I).

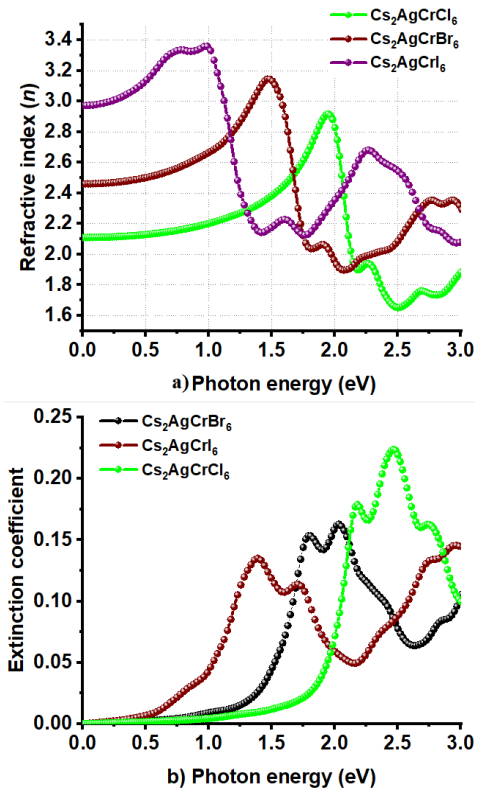

Figure 9. Behavior of the (**a**) real and (**b**) imaginary part of complex refractive index against the photon energy for Cs_2AgCrX_6 (X = Cl, Br, I).

4. Conclusions

In this study, a promising van der Waals functional called SCAN + *rVV*10 was used to theoretically investigate the electronic structures, stability, electronic, transport, and optical properties of $A_2AgCrBr_6$ (A = K, Rb, Cs). To shed some light on the effect of halogen substitution (X = Cl, I) that replaces Br in $A_2AgCrBr_6$ and for comparison, the same properties of Cs_2AgCrX_6 (X = Cl, I) obtained with the same functional were included. As such, $A_2AgCrBr_6$ (A = K, Rb, Cs) and Cs_2AgCrX_6 (X = Cl, I) were shown to exhibit a perovskite structure, emerged using the combined application of the octahedral factor, the Goldschmidt tolerance factor, and the global instability index. However, the application of the newly proposed tolerance factor τ has rejected Cs_2AgCrI_6 and $K_2AgCrBr_6$ as stable perovskites, showing its high-level predictability over the traditional ones. Despite the aforementioned rejection, each member of the series $A_2AgCrBr_6$ was shown to feature very similar bandgap properties with others, including the nature of the effective masses of charge carriers, and optical constants. Small variation in either of these properties in a given series was due to the small change in the lattice constants, cell volumes, and bonding interactions induced by alkali substitution at the A-site. The positional occurrence of the first onset of absorption which appeared in the spectra of the dielectric function, absorption coefficient, refractive index, and photoconductivity, as well as that in the Tauc plot, has demonstrated that the geometrically stable $A_2AgCrBr_6$ double perovskites emanated from this study could be interesting for their eventual experimental characterizations. We have also shown that the onset of the first absorption can be significantly shifted to the high- and low-energy infrared regions via halogen substitution at the X site with X = Cl and X = I in Cs_2AgCrX_6, respectively. Moreover, the computed electronic transitions of $Cs_2AgCrCl_6$ were shown in decent agreement with those reported experimentally for hexagonal $Cs_2AgCrCl_6$ and Cr-doped $Cs_2AgInCl_6$, meaning that the chosen computational model utilized in this study should be applicable to similar other halide double perovskites to explore similar properties. Because $A_2AgCrBr_6$ (A = Rb, Cs) and $Cs_2AgCrCl_6$ possess impressive electronic and optical properties, they are expected to find application in optoelectronics.

Author Contributions: Conceptualization, problem design, and investigation: P.R.V.; Literature survey and writing—original draft: P.R.V.; Writing—review and editing: P.R.V. The author has read and agreed to the published version of the manuscript.

Funding: The funders have no role in the conceptualization, design and publication of this work and that this research received no external funding to declare.

Acknowledgments: P.R.V. thanks Koichi Yamashita for potential technical support. This work was entirely conducted using the facilities provided by the University of Tokyo.

Conflicts of Interest: The authors declare no conflict of interest.

References

1. Matthews, P.D.; Lewis, D.J.; O'Brien, P. Updating the road map to metal-halide perovskites for photovoltaics. *J. Mater. Chem. A* **2017**, *5*, 17135–17150. [CrossRef]
2. Chu, L.; Ahmad, W.; Liu, W.; Yang, J.; Zhang, R.; Sun, Y.; Yang, J.; Li, X. Lead-Free Halide Double Perovskite Materials: A New Superstar Toward Green and Stable Optoelectronic Applications. *Nano-Micro Lett.* **2019**, *11*, 16. [CrossRef]
3. Greul, E.; Petrus, M.L.; Binek, A.; Docampo, P.; Bein, T. Highly stable, phase pure $Cs_2AgBiBr_6$ double perovskite thin films for optoelectronic applications. *J. Mater. Chem. A* **2017**, *5*, 19972–19981. [CrossRef]
4. Chen, M.; Ju, M.-G.; Carl, A.D.; Zong, Y.; Grimm, R.L.; Gu, J.; Zeng, X.C.; Zhou, Y.; Padture, N.P. Cesium Titanium(IV) Bromide Thin Films Based Stable Lead-free Perovskite Solar Cells. *Joule* **2018**, *2*, 558–570. [CrossRef]
5. Lei, L.-Z.; Shi, Z.; Li, Y.; Ma, Z.Z.; Zhang, F.; Xu, T.; Tian, Y.-T.; Wu, D.; Li, X.; Du, G.-T. High-efficiency and air-stable photodetectors based on lead-free double perovskite $Cs_2AgBiBr_6$ thin films. *J. Mater. Chem. C* **2018**, *6*, 7982–7988. [CrossRef]
6. Li, H.; Shan, X.; Neu, J.N.; Geske, T.; Davis, M.; Mao, P.; Xiao, K.; Siegrist, T.; Yu, Z. Lead-free halide double perovskite-polymer composites for flexible X-ray imaging. *J. Mater. Chem. C* **2018**, *6*, 11961–11967. [CrossRef]
7. Tan, Z.; Li, J.; Zhang, C.; Li, Z.; Hu, Q.; Xiao, Z.; Kamiya, T.; Hosono, H.; Niu, G.; Lifshitz, E.; et al. Highly Efficient Blue-Emitting Bi-Doped Cs_2SnCl_6 Perovskite Variant: Photoluminescence Induced by Impurity Doping. *Adv. Funct. Mater.* **2018**, *28*, 1801131. [CrossRef]
8. Luo, J.; Wang, X.; Li, S.; Liu, J.; Guo, Y.; Niu, G.; Yao, L.; Fu, Y.; Gao, L.; Dong, Q.; et al. Efficient and stable emission of warm-white light from lead-free halide double perovskites. *Nature* **2018**, *563*, 541–545. [CrossRef]
9. Moser, F.; Lyu, S. Luminescence in pure and I-doped AgBr crystals. *J. Lumin* **1971**, *3*, 447–458. [CrossRef]
10. Kojima, A.; Teshima, K.; Shirai, Y.; Miyasaka, T. Organometal Halide Perovskites as Visible-Light Sensitizers for Photovoltaic Cells. *J. Am. Chem. Soc.* **2009**, *131*, 6050–6051. [CrossRef]
11. Varadwaj, P. Methylammonium Lead Trihalide Perovskite Solar Cell Semiconductors Are Not Organometallic: A Perspective. *Helvetica Chim. Acta* **2017**, *100*, e1700090. [CrossRef]
12. Varadwaj, P.R.; Varadwaj, A.; Marques, H.M.; Yamashita, K. Significance of hydrogen bonding and other noncovalent interactions in determining octahedral tilting in the $CH_3NH_3PbI_3$ hybrid organic-inorganic halide perovskite solar cell semiconductor. *Sci. Rep.* **2019**, *9*, 50. [CrossRef]
13. Varadwaj, A.; Varadwaj, P.; Marques, H.M.; Yamashita, K. Halogen in materials design: Revealing the nature of hydrogen bonding and other non-covalent interactions in the polymorphic transformations of methylammonium lead tribromide perovskite. *Mater. Today Chem.* **2018**, *9*, 1–16. [CrossRef]
14. Varadwaj, P.R.; Varadwaj, A.; Marques, H.M.; Yamashita, K. Halogen in materials design: Chloroammonium lead triiodide perovskite ($ClNH_3PbI_3$) a dynamical bandgap semiconductor in 3D for photovoltaics. *J. Comput. Chem.* **2018**, *39*, 1902–1912. [CrossRef]
15. Varadwaj, A.; Varadwaj, P.; Yamashita, K. Revealing the Cooperative Chemistry of the Organic Cation in the Methylammonium Lead Triiodide Perovskite Semiconductor System. *ChemisrtySelect* **2018**, *3*, 7269–7282. [CrossRef]
16. Varadwaj, A.; Varadwaj, P.R.; Yamashita, K. Revealing the Chemistry between Band Gap and Binding Energy for Lead-/Tin-Based Trihalide Perovskite Solar Cell Semiconductors. *ChemSusChem* **2018**, *11*, 449–463. [CrossRef]

17. Varadwaj, A.; Varadwaj, P.; Yamashita, K. Hybrid organic-inorganic $CH_3NH_3PbI_3$ perovskite building blocks: Revealing ultra-strong hydrogen bonding and mulliken inner complexes and their implications in materials design. *J. Comput. Chem.* **2017**, *38*, 2802–2818. [CrossRef]
18. Zhao, X.-G.; Yang, J.-H.; Fu, Y.; Yang, D.; Xu, Q.; Yu, L.; Wei, S.-H.; Zhang, L. Design of Lead-Free Inorganic Halide Perovskites for Solar Cells via Cation-Transmutation. *J. Am. Chem. Soc.* **2017**, *139*, 2630–2638. [CrossRef]
19. Zhao, X.-G.; Yang, D.; Sun, Y.; Li, T.; Zhang, L.; Yu, L.; Zunger, A. Cu–In Halide Perovskite Solar Absorbers. *J. Am. Chem. Soc.* **2017**, *139*, 6718–6725. [CrossRef]
20. Xiao, Z.; Du, K.-Z.; Meng, W.; Wang, J.; Mitzi, D.B.; Yan, Y. Intrinsic Instability of $Cs_2In(I)M(III)X_6$ (M = Bi, Sb; X = Halogen) Double Perovskites: A Combined Density Functional Theory and Experimental Study. *J. Am. Chem. Soc.* **2017**, *139*, 6054–6057. [CrossRef]
21. Li, T.; Zhao, X.; Yang, D.; Du, M.-H.; Zhang, L. Intrinsic Defect Properties in Halide Double Perovskites for Optoelectronic Applications. *Phys. Rev. Appl.* **2018**, *10*, 041001. [CrossRef]
22. Xu, Q.; Yang, D.; Lv, J.; Sun, Y.-Y.; Zhang, L. Perovskite Solar Absorbers: Materials by Design. *Small Methods* **2018**, *2*, 1700316. [CrossRef]
23. Zhou, Y.; Askar, A.M.; Pöhls, J.-H.; Iyer, A.K.; Oliynyk, A.O.; Shankar, K.; Mar, A. Hexagonal Double Perovskite $Cs_2AgCrCl_6$. *Zeitschrift für anorganische und allgemeine Chemie* **2018**, *645*, 323–328. [CrossRef]
24. Zhao, F.; Song, Z.; Zhao, J.; Liu, Q. Double perovskite $Cs_2AgInCl_6$:Cr^{3+}: Broadband and near-infrared luminescent materials. *Inorg. Chem. Front.* **2019**, *6*, 3621–3628. [CrossRef]
25. Best Research-Cell Efficiency Chart. Available online: https://www.nrel.gov/pv/cell-efficiency.html (accessed on 25 April 2020).
26. Bagnall, K.W.; Laidler, J.B.; Stewart, M.A.A. Americium chloro-complexes. *J. Chem. Soc. A* **1968**, 133. [CrossRef]
27. Morss, L.R.; Fuger, J. Preparation and crystal structures of dicesium berkelium hexachloride and dicesium sodium berkelium hexachloride. *Inorg. Chem.* **1969**, *8*, 1433–1439. [CrossRef]
28. Morss, L.R.; Siegal, M.; Stenger, L.; Edelstein, N. Preparation of cubic chloro complex compounds of trivalent metals: Cs_2NaMCl_6. *Inorg. Chem.* **1970**, *9*, 1771–1775. [CrossRef]
29. Morrs, L.R.; Robinson, W.R. Crystal structure of $Cs_2NaBiCl_6$. *Acta Crystallogr. Sect. B Struct. Crystallogr. Cryst. Chem.* **1972**, *28*, 653–654. [CrossRef]
30. Prokert, F.; Aleksandrov, K.S. Neutron Scattering Studies on Phase Transition and Phonon Dispersion in $Cs_2NaBiCl_6$. *Phys. Status solidi (b)* **1984**, *124*, 503–513. [CrossRef]
31. Smit, W.; Dirksen, G.; Stufkens, D. Infrared and Raman spectra of the elpasolites $Cs_2NaSbCl_6$ and $Cs_2NaBiCl_6$: Evidence for a pseudo Jahn-Teller distorted ground state. *J. Phys. Chem. Solids* **1990**, *51*, 189–196. [CrossRef]
32. Flerov, I.N.; Gorev, M.V.; Aleksandrov, K.; Tressaud, A.; Grannec, J.; Couzi, M. Phase transitions in elpasolites (ordered perovskites). *Mater. Sci. Eng. R: Rep.* **1998**, *24*, 81–151. [CrossRef]
33. Jung, H.S.; Park, N.-G. Solar Cells: Perovskite Solar Cells: From Materials to Devices (Small 1/2015). *Small* **2015**, *11*, 2. [CrossRef]
34. Babayigit, A.; Ethirajan, A.; Muller, M.; Conings, B. Toxicity of organometal halide perovskite solar cells. *Nat. Mater.* **2016**, *15*, 247–251. [CrossRef]
35. Manser, J.S.; Christians, J.A.; Kamat, P.V. Intriguing Optoelectronic Properties of Metal Halide Perovskites. *Chem. Rev.* **2016**, *116*, 12956–13008. [CrossRef]
36. Zhou, Y.; Zhao, Y. Chemical stability and instability of inorganic halide perovskites. *Energy Environ. Sci.* **2019**, *12*, 1495–1511. [CrossRef]
37. Urbina, A. The balance between efficiency, stability and environmental impacts in perovskite solar cells: A review. *J. Phys. Energy* **2020**, *2*, 022001. [CrossRef]
38. Cai, Y.; Xie, W.; Teng, Y.T.; Harikesh, P.C.; Ghosh, B.; Huck, P.; Persson, K.A.; Mathews, N.; Mhaisalkar, S.; Sherburne, M.P.; et al. High-throughput Computational Study of Halide Double Perovskite Inorganic Compounds. *Chem. Mater.* **2019**, *31*, 5392–5401. [CrossRef]
39. Bartel, C.J.; Sutton, C.; Goldsmith, B.R.; Ouyang, R.; Musgrave, C.B.; Ghiringhelli, L.M.; Scheffler, M. New tolerance factor to predict the stability of perovskite oxides and halides. *Sci. Adv.* **2019**, *5*, eaav0693. [CrossRef]
40. Li, Y.; Yang, K. High-throughput computational design of organic–inorganic hybrid halide semiconductors beyond perovskites for optoelectronics. *Energy Environ. Sci.* **2019**, *12*, 2233–2243. [CrossRef]

41. Jain, A.; Voznyy, O.; Sargent, E.H. High-Throughput Screening of Lead-Free Perovskite-like Materials for Optoelectronic Applications. *J. Phys. Chem. C* **2017**, *121*, 7183–7187. [CrossRef]
42. Roknuzzaman, M.; Zhang, C.; Ostrikov, K.; Du, A.; Wang, H.; Wang, L.; Tesfamichael, T. Electronic and optical properties of lead-free hybrid double perovskites for photovoltaic and optoelectronic applications. *Sci. Rep.* **2019**, *9*, 718. [CrossRef]
43. Volonakis, G.; Haghighirad, A.A.; Milot, R.L.; Sio, W.H.; Filip, M.R.; Wenger, B.; Johnston, M.B.; Herz, L.M.; Snaith, H.J.; Giustino, F. $Cs_2InAgCl_6$: A New Lead-Free Halide Double Perovskite with Direct Band Gap. *J. Phys. Chem. Lett.* **2017**, *8*, 772–778. [CrossRef]
44. Nandha K., N.; Nag, A. Synthesis and luminescence of Mn-doped $Cs_2AgInCl_6$ double perovskites. *Chem. Commun.* **2018**, *54*, 5205–5208. [CrossRef]
45. Locardi, F.; Cirignano, M.; Baranov, D.; Dang, Z.; Prato, M.; Drago, F.; Ferretti, M.; Pinchetti, V.; Fanciulli, M.; Brovelli, S.; et al. Colloidal Synthesis of Double Perovskite $Cs_2AgInCl_6$ and Mn-Doped $Cs_2AgInCl_6$ Nanocrystals. *J. Am. Chem. Soc.* **2018**, *140*, 12989–12995. [CrossRef]
46. Karmakar, A.; Dodd, M.S.; Agnihotri, S.; Ravera, E.; Michaelis, V.K. Cu(II)-Doped $Cs_2SbAgCl_6$ Double Perovskite: A Lead-Free, Low-Bandgap Material. *Chem. Mater.* **2018**, *30*, 8280–8290. [CrossRef]
47. Chen, N.; Cai, T.; Li, W.; Hills-Kimball, K.; Yang, H.; Que, M.; Nagaoka, Y.; Liu, Z.; Yang, D.; Donga, A.; et al. Yb- and Mn-Doped Lead-Free Double Perovskite Cs_2AgBiX_6 (X = Cl^-, Br^-) Nanocrystals. *ACS Appl. Mater. Interfaces* **2019**, *11*, 16855–16863. [CrossRef]
48. Li, W.; Ionescu, E.; Riedel, R.; Gurlo, A. Can we predict the formability of perovskite oxynitrides from tolerance and octahedral factors? *J. Mater. Chem. A* **2013**, *1*, 12239. [CrossRef]
49. Goldschmidt, V.M. Die Gesetze der Krystallochemie. *Naturwissenschaften* **1926**, *14*, 477–485. [CrossRef]
50. Fedorovskiy, A.E.; Drigo, N.A.; Nazeeruddin, M.K. The Role of Goldschmidt's Tolerance Factor in the Formation of A_2BX_6 Double Halide Perovskites and its Optimal Range. *Small Methods* **2019**, *4*. [CrossRef]
51. Salinas, A.; García-Muñoz, J.L.; Rodríguez-Carvajal, J.; Sáez-Puche, R.; Martínez, J. Structural characterization of R_2BaCuO_5 (R = Y, Lu, Yb, Tm, Er, Ho, Dy, Gd, Eu and Sm) oxides by X-ray and neutron diffraction. *J. Solid State Chem.* **1992**, *100*, 201–211. [CrossRef]
52. Yamada, I.; Takamatsu, A.; Ikeno, H. Complementary evaluation of structure stability of perovskite oxides using bond-valence and density-functional-theory calculations. *Sci. Technol. Adv. Mater.* **2018**, *19*, 101–107. [CrossRef] [PubMed]
53. Dresselhaus, M.S. Solid State Physics Part II Optical Properties of Solids. 2001, Volume 6. Available online: http://web.mit.edu/course/6/6.732/www/6.732-pt2.pdf (accessed on 18 May 2020).
54. Li, L.; Wang, W.; Liu, H.; Liu, X.; Song, Q.; Ren, S. First Principles Calculations of Electronic Band Structure and Optical Properties of Cr-Doped ZnO. *J. Phys. Chem. C* **2009**, *113*, 8460–8464. [CrossRef]
55. Jong, U.-G.; Yu, C.-J.; Ri, J.-S.; Kim, N.-H.; Ri, G.-C. Influence of halide composition on the structural, electronic, and optical properties of mixed $CH_3NH_3Pb(I_{1-x}Br_x)_3$ perovskites calculated using the virtual crystal approximation method. *Phys. Rev. B* **2016**, *94*, 125139. [CrossRef]
56. Dong, L.; Jia, R.; Xin, B.; Peng, B.; Zhang, Y. Effects of oxygen vacancies on the structural and optical properties of β-Ga_2O_3. *Sci. Rep.* **2017**, *7*, 40160. [CrossRef] [PubMed]
57. Matthes, L.; Pulci, O.; Bechstedt, F. Optical properties of two-dimensional honeycomb crystals graphene, silicene, germanene, and tinene from first principles. *New J. Phys.* **2014**, *16*, 105007. [CrossRef]
58. Peng, H.; Yang, Z.-H.; Perdew, J.P.; Sun, J. Versatile van der Waals Density Functional Based on a Meta-Generalized Gradient Approximation. *Phys. Rev. X* **2016**, *6*, 041005. [CrossRef]
59. Zhang, Y.; Kitchaev, D.A.; Yang, J.; Chen, T.; Dacek, S.T.; Sarmiento-Perez, R.A.; Marques, M.A.L.; Peng, H.; Ceder, G.; Perdew, J.P.; et al. Efficient first-principles prediction of solid stability: Towards chemical accuracy. *npj Comput. Mater.* **2018**, *4*, 9. [CrossRef]
60. Buda, I.G.; Lane, C.; Barbiellini, B.; Ruzsinszky, A.; Sun, J.; Bansil, A. Characterization of Thin Film Materials using SCAN meta-GGA, an Accurate Nonempirical Density Functional. *Sci. Rep.* **2017**, *7*, 44766. [CrossRef]
61. Sun, J.; Remsing, R.C.; Zhang, Y.; Sun, Z.; Ruzsinszky, A.; Peng, H.; Yang, Z.; Paul, A.; Waghmare, U.; Wu, X.; et al. Accurate first-principles structures and energies of diversely bonded systems from an efficient density functional. *Nat. Chem.* **2016**, *8*, 831–836. [CrossRef]
62. Chakraborty, A.; Dixit, M.; Aurbach, D.; Major, D.T. Predicting accurate cathode properties of layered oxide materials using the SCAN meta-GGA density functional. *npj Comput. Mater.* **2018**, *4*, 60. [CrossRef]

63. Bokdam, M.; Lahnsteiner, J.; Ramberger, B.; Schäfer, T.; Kresse, G. Assessing Density Functionals Using Many Body Theory for Hybrid Perovskites. *Phys. Rev. Lett.* **2017**, *119*, 145501. [CrossRef] [PubMed]
64. Blöchl, P.E. Projector augmented-wave method. *Phys. Rev. B* **1994**, *50*, 17953. [CrossRef] [PubMed]
65. Kresse, G.; Furthmüller, J. Efficient iterative schemes for ab initio total-energy calculations using a plane-wave basis set. *Phys. Rev. B* **1996**, *54*, 11169–11186. [CrossRef] [PubMed]
66. Kresse, G.; Furthmüller, J. Efficiency of ab-initio total energy calculations for metals and semiconductors using a plane-wave basis set. *Comput. Mater. Sci.* **1996**, *6*, 15–50. [CrossRef]
67. Bilbao Crystallographic Server. Available online: https://www.cryst.ehu.es/ (accessed on 25 April 2020).
68. VASP Documentary on the Tetrahedron Method. Available online: https://www.vasp.at/wiki/index.php/ISMEAR (accessed on 25 April 2020).
69. Density of States Plot Using Python and Matplotlib. Available online: https://github.com/QijingZheng/pyband (accessed on 25 April 2020).
70. Ganose, A.M.; Jackson, A.; Scanlon, D.O. sumo: Command-line tools for plotting and analysis of periodic ab initio calculations. *J. Open Source Softw.* **2018**, *3*, 717. [CrossRef]
71. Böer, K.W. *Handbook of the Physics of Thin-Film Solar Cells*; Springer: Berlin/Heidelberg, Germany, 2014; ISBN 978-3-642-36747-2.
72. Gajdoš, M.; Hummer, K.; Kresse, G.; Furthmüller, J.; Bechstedt, F. Linear optical properties in the PAW methodology. *Phys. Rev. B* **2006**, *73*, 045112. [CrossRef]
73. Brivio, F.; Walker, A.B.; Walsh, A. Structural and electronic properties of hybrid perovskites for high-efficiency thin-film photovoltaics from first-principles. *APL Mater.* **2013**, *1*, 42111. [CrossRef]
74. Calculation of High Frequency Dielectric Function Using VASP. Available online: https://www.vasp.at/wiki/index.php/LOPTICS#cite_note-gajdos:prb:06-1 (accessed on 25 April 2020).
75. Perdew, J.P.; Ruzsinszky, A.; Csonka, G.I.; Vydrov, O.A.; Scuseria, G.E.; Constantin, L.A.; Zhou, X.; Burke, K. Restoring the Density-Gradient Expansion for Exchange in Solids and Surfaces. *Phys. Rev. Lett.* **2008**, *100*, 136406. [CrossRef]
76. Marzari, N.; Singh, D.J. Dielectric response of oxides in the weighted density approximation. *Phys. Rev. B* **2000**, *62*, 12724–12729. [CrossRef]
77. Corso, A.D.; Baroni, S.; Resta, R. Density-functional theory of the dielectric constant: Gradient-corrected calculation for silicon. *Phys. Rev. B* **1994**, *49*, 5323–5328. [CrossRef]
78. Kootstra, F.; De Boeij, P.L.; Snijders, J.G. Application of time-dependent density-functional theory to the dielectric function of various nonmetallic crystals. *Phys. Rev. B* **2000**, *62*, 7071–7083. [CrossRef]
79. Walsh, A. Principles of Chemical Bonding and Band Gap Engineering in Hybrid Organic–Inorganic Halide Perovskites. *J. Phys. Chem. C* **2015**, *119*, 5755–5760. [CrossRef] [PubMed]
80. Li, Y.; Yi, Y.; Coropceanu, V.; Brédas, J.-L. Optical conductivity and optical effective mass in a high-mobility organic semiconductor: Implications for the nature of charge transport. *Phys. Rev. B* **2014**, *90*, 245112. [CrossRef]
81. Yin, X.; McClary, S.A.; Song, Z.; Zhao, D.; Graeser, B.K.; Wang, C.; Shrestha, N.; Wang, X.-M.; Chen, C.; Li, C.; et al. A Cu_3PS_4 nanoparticle hole selective layer for efficient inverted perovskite solar cells. *J. Mater. Chem. A* **2019**, *7*, 4604–4610. [CrossRef]
82. Ming, W.; Shi, H.; Du, M.-H. Large dielectric constant, high acceptor density, and deep electron traps in perovskite solar cell material $CsGeI_3$. *J. Mater. Chem. A* **2016**, *4*, 13852–13858. [CrossRef]
83. Stancu, A.; Let, D.; Bacinschi, Z. CHARGE TRANSPORT IN SEMICONDUCTOR MATERIALS. *J. Sci. Arts* **2009**. Available online: http://www.josa.ro/docs/josa_2009_2/c.06_CHARGE_TRANSPORT_IN_SEMICONDUCTOR_MATERIALS.pdf (accessed on 25 April 2020).
84. Wang, Z.; Ganose, A.M.; Niu, C.; Scanlon, D.O. Two-dimensional eclipsed arrangement hybrid perovskites for tunable energy level alignments and photovoltaics. *J. Mater. Chem. C* **2019**, *7*, 5139–5147. [CrossRef]
85. Rohlfing, M.; Louie, S.G. Electron-hole excitations and optical spectra from first principles. *Phys. Rev. B* **2000**, *62*, 4927–4944. [CrossRef]
86. Onida, G.; Rubio, A.; Reining, L. Electronic excitations: Density-functional versus many-body Green's-function approaches. *Rev. Mod. Phys.* **2002**, *74*, 601–659. [CrossRef]
87. Yu, C.-J. Advances in modelling and simulation of halide perovskites for solar cell applications. *J. Physics: Energy* **2019**, *1*, 022001. [CrossRef]

88. Zakutayev, A.; Caskey, C.M.; Fioretti, A.N.; Ginley, D.; Vidal, J.; Stevanovic, V.; Tea, E.; Lany, S. Defect Tolerant Semiconductors for Solar Energy Conversion. *J. Phys. Chem. Lett.* **2014**, *5*, 1117–1125. [CrossRef]
89. Brandt, R.E.; Stevanović, V.; Ginley, D.; Buonassisi, T. Identifying defect-tolerant semiconductors with high minority-carrier lifetimes: Beyond hybrid lead halide perovskites. *MRS Commun.* **2015**, *5*, 265–275. [CrossRef]
90. Du, M.H. Hybrid organic-inorganic halide perovskites: Electronic structure, dielectric properties, native defects and the role of ns2 ions. In *Theoretical Modeling of Organohalide Perovskites for Photovoltaic Applications*; Giacomo, G., Koichi, Y., Eds.; CRC Press: Boca Raton, FL, USA, 2017; ISBN 1351648462, 9781351648462.
91. Zangwill, A. *Modern Electrodynamics*; Cambridge University Press: Cambridge, UK, 2013; Chapter 6.
92. Wilson, J.N.; Frost, J.M.; Wallace, S.K.; Walsh, A. Dielectric and ferroic properties of metal halide perovskites. *APL Mater.* **2019**, *7*, 010901. [CrossRef]
93. Hamada, Y.Z.; Bayakly, N.; Shafi, M.; Painter, S.; Taylor, V.; Greene, J.; Rosli, K. Reactions of Cr^{3+} with aspartic acid within a wide pH range. *Complex Met.* **2014**, *1*, 46–51. [CrossRef]
94. Laksman, S.V.; Devi, P.R. Optical Absorption Spectrum of Cr3+ Ion in Strontium Formate Crystal. Available online: https://www.insa.nic.in/writereaddata/UpLoadedFiles/PINSA/Vol45A_1979_4_Art11.pdf (accessed on 25 April 2020).
95. Zamyatina, E.; Karzanov, V.; Zamyatin, O. Optical properties of the zinc-tellurite glasses doped with Cr^{3+} ions. *J. Non-Crystalline Solids* **2020**, *528*, 119759. [CrossRef]
96. Pankove, J.I.; Kiewit, D.A. *Reviewer Optical Processes in Semiconductors*; Prentice Hall: Upper Saddle River, NJ, USA, 1971; p. 34.
97. Barugkin, C.; Cong, J.; Duong, T.; Rahman, S.; Nguyen, H.; Macdonald, D.; White, T.E.; Catchpole, K.R. Ultralow Absorption Coefficient and Temperature Dependence of Radiative Recombination of $CH_3NH_3PbI_3$ Perovskite from Photoluminescence. *J. Phys. Chem. Lett.* **2015**, *6*, 767–772. [CrossRef]
98. Park, N.-G. Perovskite solar cells: An emerging photovoltaic technology. *Mater. Today* **2015**, *18*, 65–72. [CrossRef]
99. Kangsabanik, J.; Sugathan, V.; Yadav, A.; Yella, A.; Alam, A. Double perovskites overtaking the single perovskites: A set of new solar harvesting materials with much higher stability and efficiency. *Phys. Rev. Mater.* **2018**, *2*, 055401. [CrossRef]
100. Ezealigo, B.N.; Nwanya, A.C.; Ezugwu, S.; Offiah, S.; Obi, D.; Osuji, R.U.; Bucher, R.; Maaza, M.; Ejikeme, P.; Ezema, F.I. Method to control the optical properties: Band gap energy of mixed halide organolead perovskites. *Arab. J. Chem.* **2020**, *13*, 988–997. [CrossRef]
101. Chen, C.-W.; Hsiao, S.-Y.; Chen, C.-Y.; Kang, H.-W.; Huang, Z.-Y.; Lin, H.-W. Optical properties of organometal halide perovskite thin films and general device structure design rules for perovskite single and tandem solar cells. *J. Mater. Chem. A* **2015**, *3*, 9152–9159. [CrossRef]
102. He, C.; Zha, G.; Deng, C.; An, Y.; Mao, R.; Liu, Y.; Lu, Y.; Chen, Z. Refractive Index Dispersion of Organic–Inorganic Hybrid Halide Perovskite $CH_3NH_3PbX_3$ (X=Cl, Br, I) Single Crystals. *Crystal (Wiley)* **2019**, *54*, 1900011.